Multifunctional and customizable lattice structures for simultaneous sound insulation and structural applications

Xinwei Li [a], Miao Zhao [b], Xiang Yu [c], Jun Wei Chua [b], Yong Yang [d], Kian Meng Lim [b,*], Wei Zhai [b,*]

[a] Mechanical Engineering, Newcastle University, Singapore 567739, Singapore
[b] Department of Mechanical Engineering, National University of Singapore, 117575, Singapore
[c] Department of Mechanical Engineering, The Hong Kong Polytechnic University, 999077, Hong Kong Special Administrative Region
[d] Temasek Laboratories, National University of Singapore, 117411, Singapore

ARTICLE INFO

ABSTRACT

With noises being omnipresent in the modern society, sound-insulating materials are implemented in almost all walks of life. For implementations in practical applications, those that are air-ventilating and mechanically robust are highly sought-after. Herein, we present a novel concept of using lattice structures as potential ventilated sound-insulating structural materials. Focusing on a superimposed tubular and plate morphology, using a defined geometrical factor, a wide range of elastic properties can be achieved. For the isotropic lattice consisting of three layers at a cell size of 20 mm, experimentally measured, a maximum sound attenuation occurs at 1810 Hz with a high intensity of 32 dB. Past 5000 Hz, another strong attenuation band appears. Being porous, the lattice is highly ventilating with 35% of the airflow retainable. Through numerical simulations, the attenuation mechanisms are found to attribute to local Helmholtz resonance and Bragg scattering, successively. Discretizing the lattice microstructure, we propose a microstructure-based analytical model that can be used to predict and design the transmission properties of lattices. Through these, we thus come up with an overall sound transmissibility and mechanical property map based on geometrical factors. Overall, we show the potential of lattice structures as multifunctional sound-insulating materials.

1. Introduction

Amongst the various forms of daily environmental health hazards, noises are amongst the most avoidable if proper engineering control measures are implemented. For instance, noises arise from construction, traffic, machinery, and daily activities, etc. In these open environments, sound barriers, or sound-insulating materials, are needed. Indeed, they are commonly observed to be planted around construction sites, along railway tracks, covering heavy machinery, etc. Commonly adopted traditional and commercial sound insulating materials often take on the form of dense fabric, perforated panels, sandwich panels, and fully solid panels (Fig. 1A). They are often non-ventilating, i.e., they do not allow airflow across them effectively. However, for practical applications, such materials are oft-required to be ventilating. For instance, the sound barrier around heavy machinery needs to be ventilated to allow heat exchange and cooling. Internally built-up heat would result in

overheating risks of the machine. Also, closed windows are highly sound-insulating. However, closed windows impede airflow into and out of the room, rendering it non-ideal for the inhabitants inside. Therefore, numerous research efforts have been placed on ventilated sound-insulating materials and structures [1], particularly on acoustic metamaterials [2]. To adhere to the principles of acoustics, the size of an acoustic structure should closely match the wavelength associated with the noise frequency. However, acoustic metamaterials stand out because they can provide effective sound insulation even when their size is much smaller than the wavelength, achieved by modification of the transmission pathway [2].

Leveraging the Bragg scattering mechanism, many research efforts have been placed on sonic crystals acoustic metamaterials – the periodic arrangement of features that enables sound wave attenuation based on the destructive interference of scattered waves (Fig. 1B). This periodic arrangement thus allows such a material to be porous with air

flowability. Sonic crystal consists of any elements, usually columnar, arranged periodically [3]. Modifications include introducing micro-perforated panels [4] and *meta*-structures [5] into the crystal elements to introduce additional sound attenuation mechanisms into the material. Another class of prominent ventilated sound barrier include acoustic metamaterials based on local resonance (Fig. 1B), in particular, cavity, Helmholtz, and Mie resonance mechanisms. These sound insulators include micro-perforated panels [6], labyrinthine structures [7], archi-tectured cavities [8–11], etc. Researchers have also transformed them into a kind of *meta*-cage, a ventilated sound-insulating box based on an assembly of local resonators [10–12]. The morphology and mechanism of sonic crystals and local resonators are reminiscent of an advanced type of metamaterial based on lattice structures. Defined to be any three-dimensional spatially architectured porous solid, lattice structures are attracting increasing research interest for their high customizability and unprecedented physical properties. Lattice structures have thus been widely studied as lightweight structural materials [13,14], energy ab-sorbers [15], and materials with *meta*-behaviours [16,17], etc. Recently,
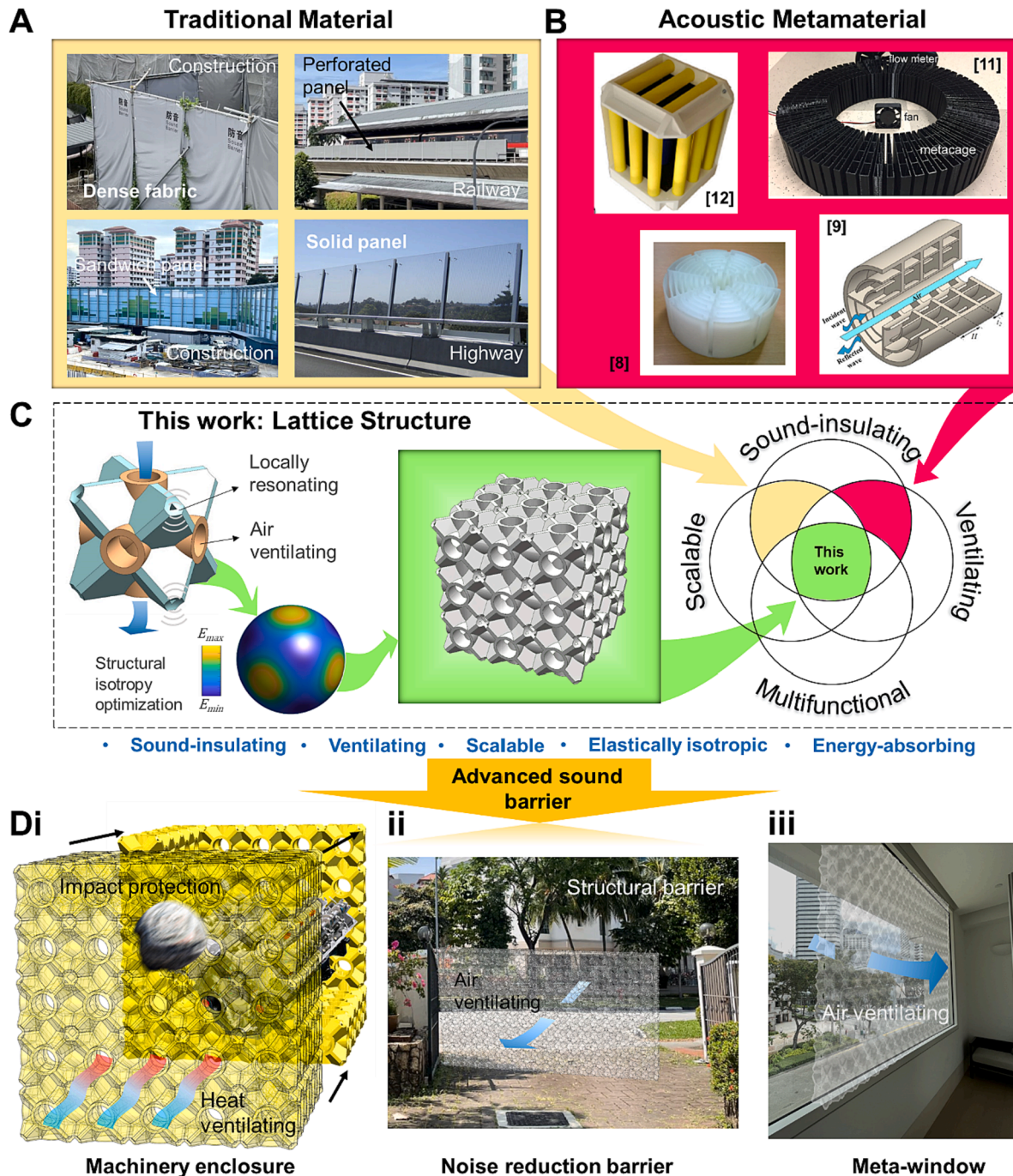

Fig. 1. An overall schematic of sound insulating materials and potentials of our lattice structure. Examples of (A) traditional and commercial materials implemented for sound insulation and (B) acoustic metamaterial proposed as ventilated sound insulators. Image of metamaterial 8 reproduced with permission from Ref. [8], Springer Nature. Image of metamaterial 9 reproduced with permission from Ref. [9], Elsevier. Image of metamaterial 11 reproduced with permission from Ref. [11], AIP Publishing. Image of metamaterial 12 reproduced with permission from Ref. [12], Acoustical Society of America. (C) Our proposed lattice structure, and an illustration of its advantages as compared to traditional materials and acoustic metamaterials. (D) Illustrations of some examples of the applications of our lattice structure, (i) as a machinery enclosure, (ii) as structural barrier along roadside, and (iii) as a ventilated *meta*-window.

lattice structures have also been attracting profound research interest in acoustics as sound absorbers [18–23]. Their potential as effective sound absorbers are revealed from the high and broadband sound absorption coefficient curves obtained. Further, the presence of resonance mechanisms in the structures of lattices has been confirmed. For instance, plate structures with pores [18,21,24–26] and dense truss lattices [18,22] are characteristic Helmholtz resonators for their distinct pore-and-cavity morphology. Resonance based on the cavity geometry has also been observed in hollow truss-lattices [20]. Alternatively, composite lattices with damping phases are possible [27].

However, thus far, no study has been carried out to investigate the potential of lattices as sound insulators. As compared to previously reported sonic crystals and acoustic metamaterials, lattices are advantageous in terms of high geometrical design freedoms and fully tuneable physical (including acoustics) properties [28]. This thus implies customizable designs for on-demand sound attenuation control in specified frequency bands and intensities under different working environments. This potential has been revealed for lattice lattices designed for sound absorption applications [29]. Apart from this, lattice structures are also advantageous as multifunctional materials, as opposed to sonic crystal or other types of metastructures. Prior mentioned, lattice structures are excellent lightweight materials and energy absorbers. Thus, lattice sound insulators can effectively dual-function as a structural material. This promotes materials usage efficiency, i.e., one material used as opposed to more, which thus translates to improved energy conversion efficiencies and/or sustainability. Indeed, researchers have leveraged this and introduced multifunctional sound-absorbing and energy-absorbing lattice structures [18,19,21]. On the contrary, acoustic metamaterials are not mechanically robust and they are non-scalable for adaptive uses as a material. For both traditional insulators and acoustic metamaterials, they can only be limited to being part of the architectural design, as opposed to being a material with dynamic functionalities. As such, lattice structures display the potential of overcoming all the above-mentioned limitations associated with traditional materials and acoustic metamaterials.

Therefore, in this work, we present a new type of tube and plate hybrid lattice structure with effective sound insulation capabilities (Fig. 1C). Following the fundamental design concept, we have also optimized the lattice to achieve elastic isotropy. Being elastically isotropic, the lattice can thus be implemented as a structure or energy absorber in a general working environment, as opposed to the highly anisotropic ones in a predictable environment. Overall, at a unit cell size of 20 mm, with three cells through thickness, the maximum sound transmission loss measures to be 32 dB, at a frequency around 1810 Hz. Following the first maximum, the region with losses above 10 dB corresponds to a broad range of frequencies from 1440 to 1950 Hz. From 5000 Hz onwards, another broad attenuation maximum occurs. Numerically analyzed, the first attenuation band attributes to local resonance mechanism while the second attributes to Bragg scattering. Being a porous material, the barrier is also highly air-ventilating with 35% of the airflow retainable. A sound transmission gap design guide, based on cell sizes, is also proposed. Our lattice structure is thus a multifunctional ventilated sound insulator and lightweight material, customizable for various applications (Fig. 1D).

2. Materials and methods

2.1. Structural simulation and homogenization

Mechanical finite element modelling (FEM) and structural optimization were carried out using Abaqus/Standard. Being periodic, the RVEs, with periodic boundary conditions (PBC) being applied, were then adopted for investigations. To impose PBC on the RVE, symmetry of the meshes on the parallel faces must be ensured. To achieve this, an eighth of the RVE is first meshed, after which, symmetry operations were then carried out to complete meshing the entire unit (Fig. S1,

Supplementary Materials). Following this, the RVEs were then imposed with PBC, using the multi-point constraint function in Abaqus, via the relationship [30]: $u_i^{k+} - u_i^{k-} = \varepsilon_{ij}\left(y_j^{k+} - y_j^{k-}\right) = \varepsilon_{ij}L_j$. u_i refers to the displacement field, ε_{ij} to the strain, L_j the periodic length (also the cell size), and k + and k- refer to the two pairs of parallel faces normal to the k-direction (k = 1, 2 or 3), respectively.

For any material, the general form of Hooke's law is given as:

$$\sigma_{ij} = C_{ijkl}\varepsilon_{kl} \tag{1}$$

In terms of the Voigt's notation, where $[\sigma_{11}\ \sigma_{22}\ \sigma_{33}\ \sigma_{23}\ \sigma_{12}\ \sigma_{13}]^T = [\sigma_1\ \sigma_2\ \sigma_3\ \sigma_4\ \sigma_5\ \sigma_6]^T$, and $[\varepsilon_{11}\ \varepsilon_{22}\ \varepsilon_{33}\ 2\varepsilon_{23}\ 2\varepsilon_{12}\ 2\varepsilon_{13}]^T = [\varepsilon_1\ \varepsilon_2\ \varepsilon_3\ \varepsilon_4\ \varepsilon_5\ \varepsilon_6]^T$, the stiffness tensor, C_{ijkl}, of a cubic symmetry material can be represented using:

$$\begin{bmatrix} \sigma_1 \\ \sigma_2 \\ \sigma_3 \\ \sigma_4 \\ \sigma_5 \\ \sigma_6 \end{bmatrix} = \begin{bmatrix} C_{11} & C_{12} & C_{12} & 0 & 0 & 0 \\ C_{12} & C_{11} & C_{12} & 0 & 0 & 0 \\ C_{12} & C_{12} & C_{11} & 0 & 0 & 0 \\ 0 & 0 & 0 & C_{44} & 0 & 0 \\ 0 & 0 & 0 & 0 & C_{44} & 0 \\ 0 & 0 & 0 & 0 & 0 & C_{44} \end{bmatrix} \begin{bmatrix} \varepsilon_1 \\ \varepsilon_2 \\ \varepsilon_3 \\ \varepsilon_4 \\ \varepsilon_5 \\ \varepsilon_6 \end{bmatrix} \tag{2}$$

From Eq. (2), it is clear that cubic material is sufficiently described using three independent stiffness constants: C_{11}, C_{12}, and C_{44}. Through FEM, C_{11}, C_{12}, can be derived using a strain load in the ε_1 direction, while C_{44} is in turn obtained from a strain load in the ε_4 direction. The Young's modulus (E), shear modulus (G), and Poisson's ratio (υ) for a cubic symmetry material are then calculated through the following transformations:

$$E = \frac{C_{11}^2 + C_{11}C_{12} - 2C_{12}^2}{C_{11} + C_{12}} \tag{3}$$

$$G = C_{44} \tag{4}$$

$$v = \frac{C_{12}}{C_{11} + C_{12}} \tag{5}$$

For an isotropic material, where $G = E/[2(1+v)]$, a measure of the degree of deviation from isotropy for an orthotropic material is thus often expressed using the ratio of G and $E/[2(1 + v)]$. Simplifying the ratio in terms of the three elastic constants, this hence constitutes the Zener's ratio (A):

$$A = \frac{2C_{44}}{C_{11} - C_{12}} \tag{6}$$

This thus implies that an isotropic material will display a Zener's ratio of 1 while increased anisotropy becomes either increasingly larger or smaller than 1, depending on the directional dominance. We thus adopt the Zener's ratio as a standard for measuring isotropy herein. Material properties, based on that of the 3D printed rigid polymer, were adopted for modelling: Young's modulus of 2.7 GPa, Poisson's ratio of 0.3, and density of 1.18 g/cm³.

2.2. 3D printing

All of the samples were 3D printed using the Asiga Max X27 vat photopolymerization 3D printer (Asiga, Australia). The rigid polymer resin used is NovaStan, from Nova3D, and the tough polymer resin used is PlasClear V2, from Asiga. The key printing parameters for NovaStan are as follows: digital light intensity of 5 mW/cm², layer thickness of 100 μm, layer exposure of 1.5 s. The key printing parameters for PlasClear V2 are as follows: digital light intensity of 35 mW/cm², layer thickness of 100 μm, layer exposure of 3.5 s. For both types of materials, the as-printed parts are then thoroughly washed in isopropyl alcohol and subsequently post-cured in the Asiga Flash ultraviolet curing chamber for 2 h.

2.3. Compression property measurements

Quasi-static compression tests were carried out using the Shimadzu AG-25 TB universal testing machine using a 50 kN compression load cell. Compliance correction, in accordance to methods described in literature [31], was carried out to account for the machine compliance that give rise to inaccuracies in the measured strain. Details on the dimensions of the compression test samples are given in Fig. S2.

2.4. Sound transmission loss measurements

The four-microphone technique using the impedance tube was adopted herein to measure the sound transmission loss properties of the samples. The BSWA SW series impedance tube, with the BSWA MPA416 microphone, and data processing software VA-Lab, from BSWA Tech, were used herein. For the frequency range from 200 to 1900 Hz, a 100 mm tube is adopted. For the further range from 1900 to 6500 Hz, a 30 mm tube is adopted. The samples are ensured to snug-fit inside the tubes.

2.5. Acoustics modelling

The analytical sound transmission loss model was modelled in Matlab. FEM analysis of acoustic properties was carried out using COMSOL Multiphysics. Our FEM model is essentially based on a mimicry of the actual experimental setup, as shown in Fig. S3. The Pressure Acoustics and Thermoviscous Acoustics modules were adopted to model the air pressure transfer through the impedance tube and the solid lattice, and the air phase within the lattice, respectively. The built-in material properties of air in COMSOL were adopted to model the air phases. For the lattice, the solid material with a density of 1.18 g/cm^3 and speed of sound through the material of 1500 m/s were adopted. The sound pressure levels were then mapped using the innate *ta.Lp* function of the Thermoviscous Acoustics module. The STL curve is calculated via the relationship: $STL = 10\log_{10}(P_{in}/P_{out})$ across the desired range of frequencies. P_{in} and P_{out} refer to the pressure of the sound source, and upon exit of the material, respectively. P_{in} and P_{out} are calculated by performing a surface integration. The band structure analysis was carried out also using COMSOL Multiphysics. The Pressure Acoustics physics, under the Floquet boundary conditions, were applied to the RVE of the Iso-PTH for sound transmission properties. For the STL investigations along [1 0 0], a scan of the k-vector from [0 0 0] to [π/L 0 0] was carried out to achieve the band structure along this direction.

3. Results and discussion

3.1. Design and elastic properties

In this work, we base our design on several considerations: (i) ventilated structure for airflow, (ii) sound attenuation mechanisms, and (iii) potentials for high strength and elastic isotropy. Therefore, we have then come up with an empirically derived hybrid structure consisting of simple cubic (SC) tubes, and face-centered cubic (FCC) plates with pores (Fig. 2**A**). The highly open structure of the SC tubes contributes to air ventilation while the FCC plates (with pores) contribute to both high mechanical rigidity and local resonance mechanisms [32]. Schematically illustrated, the FCC plate is added onto the outer shell of the SC tube while keeping the inner of the SC tube hollow. Considering the unit cell length to be L, pores in the FCC plate are then introduced by subtracting a sphere of 0.3L diameter from the corners of the FCC plate structure. This results in a structural morphology associated with a local resonance mechanism that meanwhile ensures printability [18,21]. The SC tubes and FCC plates have the same wall thickness. The relative density, ρ*, of the lattice is then tuned by changing both wall thickness concurrently. Primary geometrical features of interest include the ratio of the inner diameter, D, of the SC tube, to the unit cell length, L. We
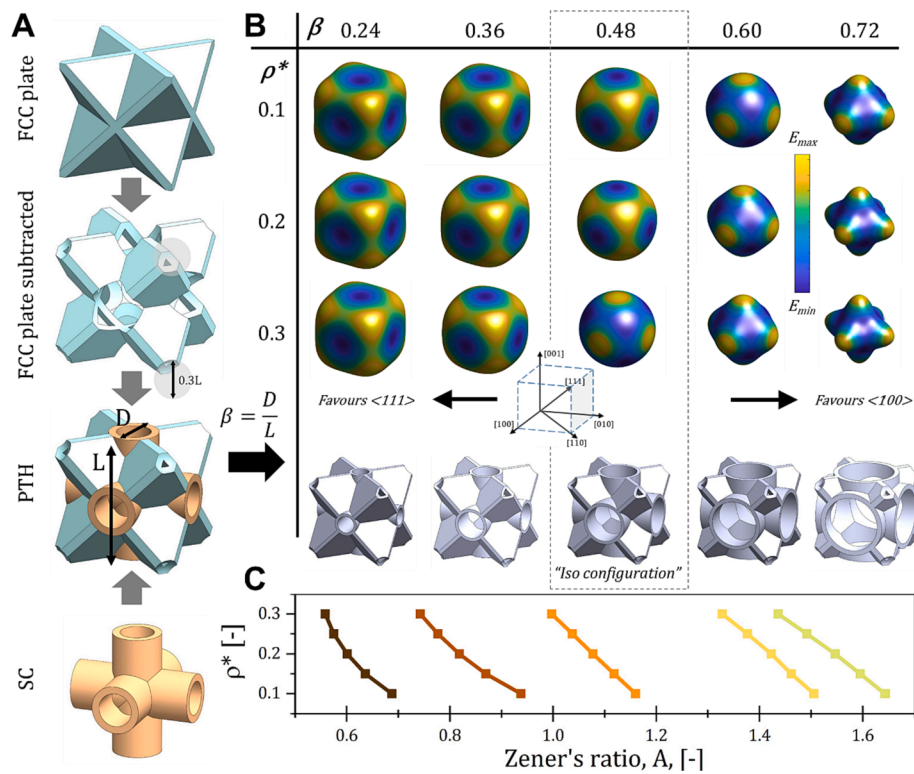

Fig. 2. Structure design and optimization. (A) The schematic of the PTH lattice design, based on combining FCC plates and SC tube constituents. (B) The elastic isotropy surfaces of PTH lattices with a range of β and ρ* values. Coordinates used for illustration, and the color scalebar, are depicted in the same figure. (C) The plot of Zener's ratio, with respect to β and ρ*.

then leverage this ratio for use as a structural factor, β, for the structural optimization of the lattice:

$$\beta = D/L \qquad (7)$$

β essentially controls the proportions of the SC tube and FCC plate phases. For instance, from Fig. 2**B**, it is apparent that a low β leads to a more FCC-based structure, and vice versa for a high β. By adjusting this parameter, an isotropic combination can then be realized. Being elastically isotropic, the lattice can thus be implemented as a structural member or an energy-absorbing material in a general working environment, as opposed to the directional ones in a predictable environment. For namesake convenience in the subsequent sections, nomenclature of this new class of plate-tube hybrid lattice is abbreviated as PTH, suffixed by its structural factor. Herein, we adopt the homogenization method, based on RVE, to optimize the lattice structure for elastic isotropy. Through FEM, we are able to obtain the elastic constants and the Zener's ratio of the orthotropic material.

Investigations were carried out for the range of structures with β of (0.24, 0.36, 0.48, 0.6 and 0.7) and ρ* of (0.1, 0.2, 0.3). Fig. 2**B** shows the elastic surfaces, expressed in terms of the maximum and minimum Young's modulus, of an RVE (also the unit cell) of these structures. The more "spherical" the elastic surface, the better the elastic isotropy is. From a β of 0.24 to 0.72, a transition from a "cubic" structure to a "cross"-like structure is observed. Under the coordinate system shown in the same figure, this suggests that low β structures are strong in the [1 1 1] direction while high β structures are strong in the [1 0 0] directions. Not surprising, these observations attribute to the proportion of the structures. A high β corresponds to a SC tube dominated structure where most of the materials are axially aligned in the [1 0 0] direction while a low β corresponds to an FCC plate dominated structure where stronger localization is observed in the [1 0 0] direction [33]. At a transition stage, with β = 0.48, near-isotropic structures can be realized. The highest isotropy is observed at ρ* = 0.3 while it reduces with decreasing ρ*. Nonetheless, it can be said to be almost isotropic throughout the investigated range of relative densities. For the structure with β of 0.48, we term it as the Iso-PTH. Figuratively, a plot of the Zener's ratio with respect to β and ρ* is shown in Fig. 2**C**. From the definition of the Zener's ratio (Section S2), an isotropic material will display a Zener's ratio of 1 while increased anisotropy becomes either increasingly larger or smaller than 1, depending on the directional dominance. Also, it is revealed that Iso-PTH display A values extremely close to 1. The relationships between E, β and ρ*, and detailed explanations of the stress distributions for the whole range of β are summarized in Fig. S4, 5. Next, we benchmark the performance of the Iso-PTH to the Hashin-Shtrikman upper bounds (HSU) for a two-phase isotropic material. Calculations for the HSU are detailed in Section S2 [32]. The normalized E, G, and bulk modulus (K), across a range of ρ* from 0.1 to 0.3, of the Iso-PTH are plotted in Fig. 3**A**. Generally, it can be observed that the Iso-PTH falls within 50–60% of the HS upper bounds. As compared to isotropic trusses, the Iso-PTH also displays superior mechanical properties [34]. This then attributes to the superior load-bearing capabilities of the approximate-membrane stress in the plates and the deformation resistance of the tube of the Iso-PTH, as opposed to the tension and compression of struts [34].

3.2. Compressive properties

To experimentally validate the elastic isotropy, we next carry out compression tests on 3D printed samples of the Iso-PTH. We investigate its compression responses in two major cubic directions: [1 0 0] and [1 1 0]. The smallest repeating unit cell in each of these directions are shown in Fig. 3**Bi**. The samples are 3D printed via digital light processing using two types of polymers. An illustration of the printed samples is shown in Fig. 3**Bii**. Fig. 3**Ci** shows the representative compressive stress–strain curves of the samples fabricated using a rigid polymer.

Indeed, the Young's modulus measured for [1 0 0] and [1 1 0] samples agree well with each other and no discernible differences between them have been observed. A typical value measure to be 287 MPa. Where the bulk polymer displays a Young's modulus of 2.7 GPa, this also agrees well with the theoretical value of 311 MPa, calculated using the theoretical relations that were established (Fig. 3**A**). Fabricated using a rigid polymer, the samples display high stiffness and strength, albeit at the expense of toughness as observed from the early onset of fracture. However, fabricated using a tough polymer, the samples instead display energy absorption behaviours as characterized by their long and flat stress plateaus (Fig. 3**Cii**). The specific energy absorption values, calculated by integrating the area under the stress–strain curve up to densification (ε_d), measure to be 2.1 and 2.5 J/g for the [1 0 0] and [1 1 0] samples, respectively. Also, where the bulk polymer displays a Young's modulus of 1.2 GPa, the measured Young's modulus of 105 MPa agrees well with the theoretical value of 138.6 MPa. Deviations observed between the experimentally measured and numerical values then attribute to the defects arising from the vat-polymerization 3D prints [30]. These results affirm the validity of our elastic isotropy optimization.

3.3. Sound transmission loss performance

Following discussions on mechanical properties, we next demonstrate the sound insulation capabilities of the Iso-PTH. For the sound transmission loss (STL) investigations, we adopt the Iso-PTH with ρ* = 30%, L = 20 mm, and the entire sample consists of three unit cells through thickness. The STL curve of the Iso-PTH, measured using the impedance tube technique, is shown in Fig. 4**A**. As observed, the sample displays a characteristic resonance peak at the low frequency range (around 1800 Hz) and a high attenuation region past 5000 Hz. For the resonance peak, maximum attenuation takes place at 1810 Hz with a magnitude of 32 dB. Within this peak, there is also a broad region of 510 Hz with an effective insulation higher than 10 dB, at the frequency range of 1440–1950 Hz (the inset in Fig. 4**A**). Beyond this first resonance peak, a second high insulation region takes places from around 5000 Hz onwards. The abovementioned performance is remarkable considering that the structure is air ventilating – a quality highly desired for various practical engineering applications. As a proof of concept, airflow experiments were then conducted. Fig. 4**B** shows the cases with, and without the Iso-PTH in the way of the airflow source and the flow meter. Under an airflow of 4 m s^{-1}, under the Iso-PTH insulation, 35% of the airflow is still retained as measured using the flow meter. This implies good ventilation in this structure.

3.4. Sound attenuation mechanisms

3.4.1. Local resonance and Bragg scattering

We next macroscopically illustrate the attenuation mechanisms through FEM analysis on the sound pressure levels (SPL) of the wave propagation across the sample. The FEM modelled STL curve, along with the experimental one superimposed, is shown in Fig. 4**C**. As observed, the two curves are in good agreements with one another. To sufficiently depict the SPL across the structure, we designate two types of cross-sectional cut planes for observations (Fig. 4**D**). The (1 0 0) plane, which lies on the face of a unit cell, illustrates the SPL transformation through the narrow pore and wide cavity of the FCC plate section. The (2 0 0) plane, which lies as a plane in the middle of a unit cell, illustrates the SPL transformation through the hollow SC tubes. Using these sections for illustrations, the cross-sectional cut planes of the Iso-PTH, at selected frequencies: 500, 1800, and 5000 Hz, are shown in Fig. 4**E**. With respect to the STL curve (Fig. 4**A**), these correspond to the regions with weak sound insulation, the first resonance peak, and the second increase in insulation, respectively. The SPL, expressed using a colormap, is then annotated using the colorbar in the same figure. As observed for both planes, at 500 Hz, only a slight decay in the SPL, characterized by a small gradient in the color scheme, is observed through the structure. The
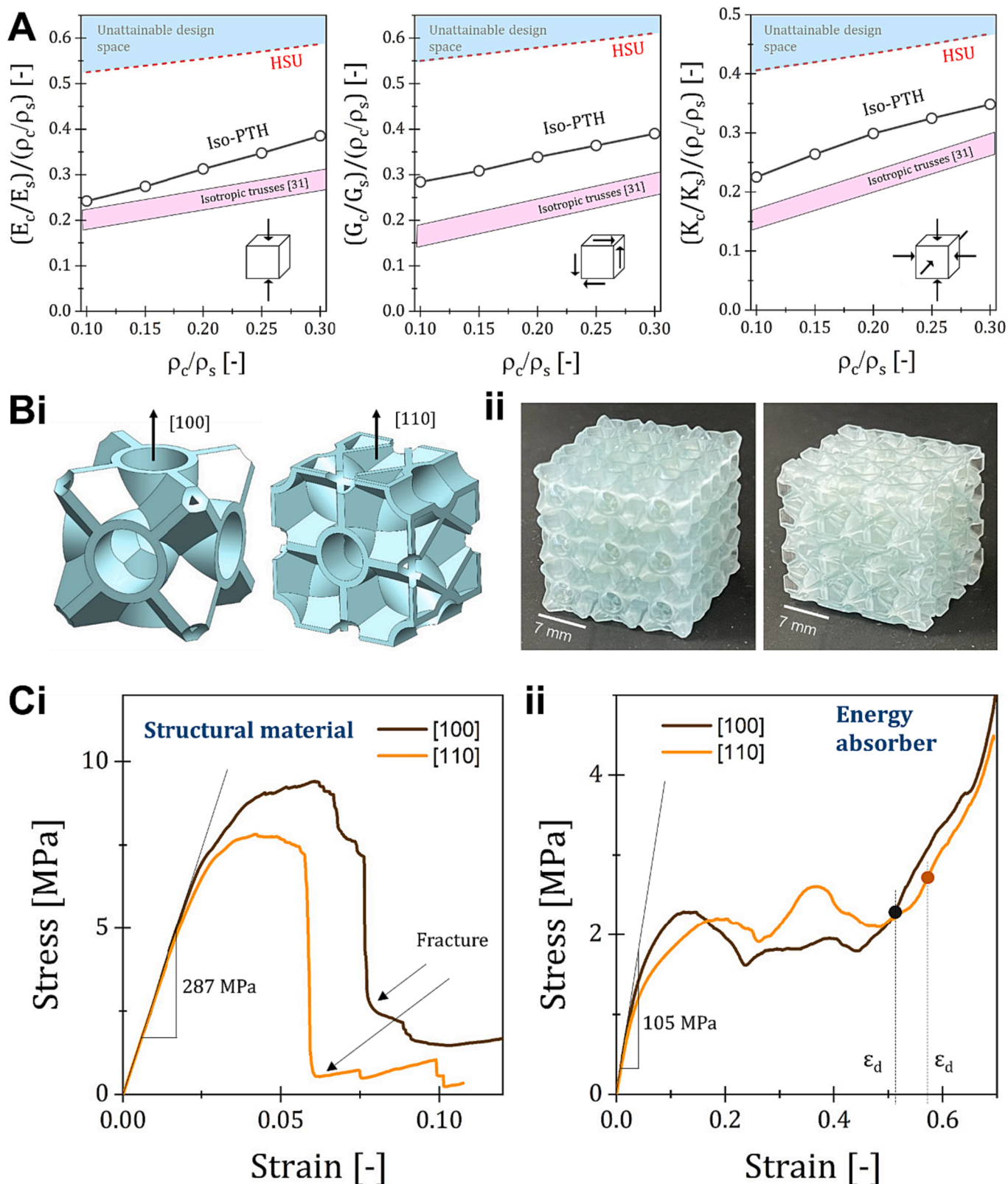
Fig. 3. Mechanical properties of the Iso-PTH. (A) E, G, and K, of the Iso-PTH, as compared to that of the HSU and isotropic trusses. (Bi) An illustration of the unit cells along the [1 0 0] and [1 1 0] directions, and (ii) their 3D printed counterparts. The representative compressive stress–strain curves of the Iso-PTHs made using (Ci) a rigid polymer and (ii) a tough polymer. The measured Young's moduli are illustrated onto the same figure.
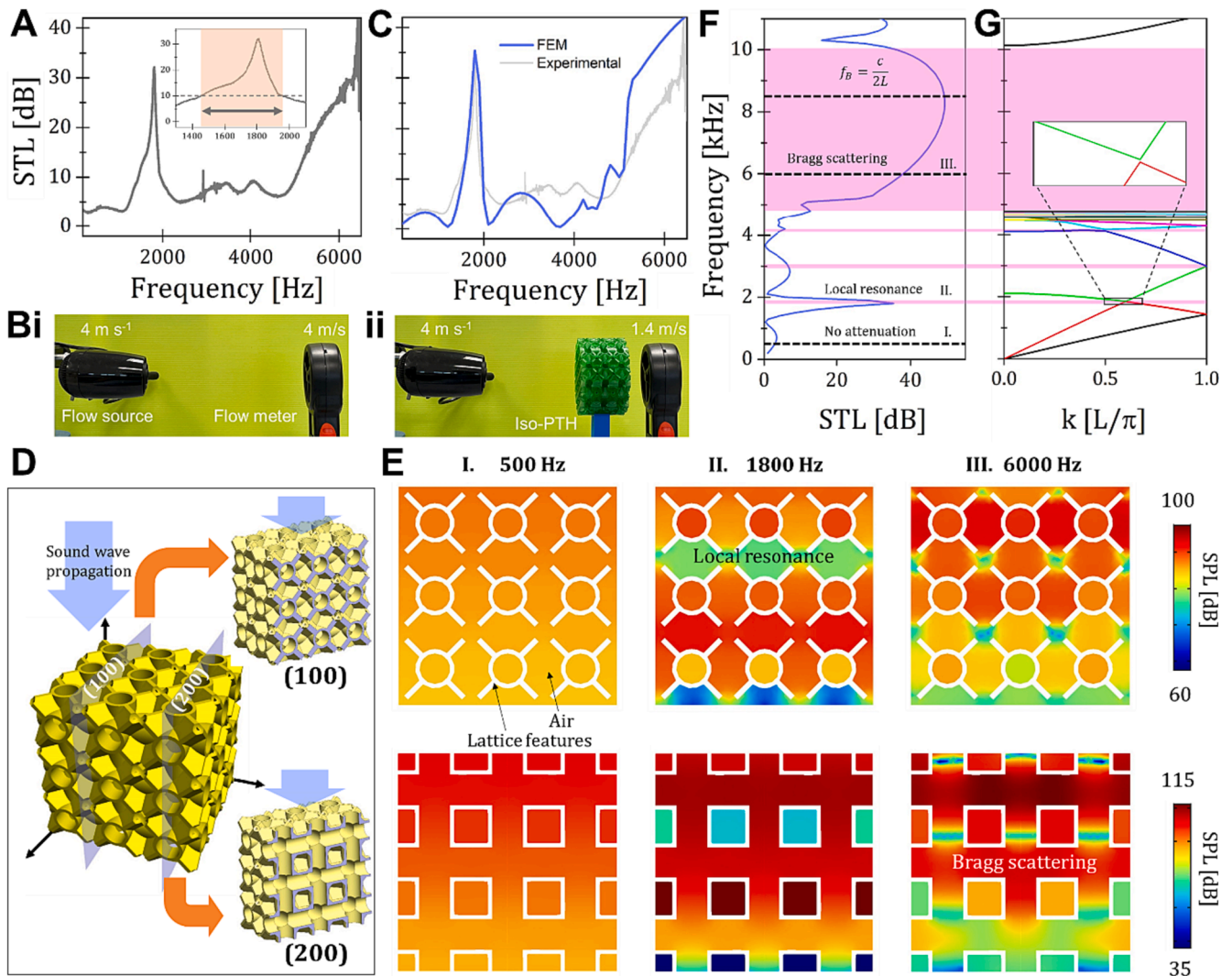
Fig. 4. Sound transmission properties of the Iso-PTH. (A) The experimentally measured STL curve of the Iso-PTH. The inset shows the zoomed in view of the STL curve, revealing the band with a high transmission above than 10 dB. (B) The FEM modelled STL curve, and as compared to that experimentally measured. (C) The airflow experiments, revealing the measured airflow in direct contact with the flow source, and with an Iso-PTH in between. (D) A schematic of the cross-sectional cut planes chosen to illustrate the SPL through the lattice. (E) The color distribution map of the SPL, on the selected (100) and (200) planes, at various frequencies: 500, 1800, and 6000 Hz. The (F) modelled STL curve and the (G) band diagram at normal sound incidence. The inset in (G) gives a clear magnified view of the narrow bandgap.

structure is nearly acoustic transparent at 500 Hz. Large variations are in turn observed at 1800 Hz. For the three-layered Iso-PTH, the highest drop in SPL occurs immediately following the first layer of cells. This occurs at the narrow regions as observed in the (100) plane and the wide cavities as observed in the (200) plane. The sound pressure is notably concentrated in the narrow pores, a typical feature of local resonance mechanisms. This drop in pressure aligns with the characteristics of local resonance mechanisms. In the case of this structure with narrow pores and wide cavities, its morphology bears resemblance to that of a Helmholtz resonator. Indeed, calculated using the Helmholtz resonance equation [18]:

$$f_h = \frac{c}{2\pi}\sqrt{\frac{A}{Vt}} \tag{8}$$

where c refers to the speed of sound, A to the surface area of the pore, V to the volume of the cavity and t to the thickness through an entire narrow pore, f_h with a value of 1874 Hz matches well with the resonant frequency observed herein. Details on the geometrical parameters herein are supplemented in Fig. S6. Thus, it is also worth noting that the resonant frequency under the local resonance mechanism is

independent on the number of layers in the direction of sound wave propagation. Instead, the intensity of transmission loss increases with increasing thickness [35]. Within the framework of the local resonance mechanism, the decrease in SPL can be attributed to the reduction in sound wave energy, as the sound waves undergo vigorous resonance, leading to energy loss through frictional and thermal losses. Again, a vastly different pattern is in turn observed at 5000 Hz. Most clearly observed from the (200) plane, distinct wave fronts, in the direction of wave propagation, of low SPL spread through the structure. Towards the exit of the lattice, these wavefronts interact with one another and their SPL intensity further decreases. Observations in the (100) plane essentially parallels that in the (200) plane. This SPL pattern is a distinctive characteristic of Bragg scattering effects originating from periodicity, e.g., the periodic lattice structure herein [36]. The decrease in SPL observed upon exiting the Iso-PTH results from the destructive interference of out-of-phase sound waves. Owing to the measurement limitations of the impedance tube, the acoustic behavior at extremely high frequencies, e.g., beyond 6500 Hz, is then modelled through simulation. With high correlation between the experimental and FEM curves within the lower frequency range (Fig. 4C), we therefore present

the FEM curve, within the whole frequency range, with confidence (Fig. 4F). Indeed, as expected, an extremely broad peak with high STL is observed. The central frequency of the peak, at around 8000 Hz, then corresponds to that calculated using the Bragg equation given by $f_B = c/2L$ [37]. This further reinstates the mechanism to be due to Bragg scattering. Also modelled using COMSOL, the band diagram of the Iso-PTH from the wavevector (L/π) of 0 to 1, in the direction of sound wave propagation, is shown (Fig. 4G). Bandgaps, at frequencies corresponding to the maximum attenuation in the STL curve, have been observed. It is to note that apart from the gaps around 1810 Hz and the Bragg frequency, minor gaps have also been observed around 3000 and 4200 Hz. They have not contributed significantly to sound attenuation at their respective frequencies, as observed from the STL curves in Fig. 4A.

3.4.2. Microstructural analysis and analytical model

Following overview of the through FEM studies, we next propose a microstructure-based analytical model for the STL properties of the Iso-PTH. The model is achieved by discretizing the acoustic impedance of fundamental units and calculating the overall acoustic impedance. The Iso-PTH is discretized as shown in Fig. 5A. From the same figure, it can be seen that a unit of the lattice consists of (i) a region of alternating narrow pores and wide cavities, and (ii) a hollow tube. Sound transmission thus consists of two parallel paths. Herein, we derive the numerical solution using the transfer matrix method (TMM). The TMM links the acoustic pressure, P, and velocity, U, on the inlet, x = 0, and outlet side, x = NL, of the material:

$$\begin{bmatrix} P \\ U \end{bmatrix}_{x=0} = T_P \begin{bmatrix} P' \\ U' \end{bmatrix}_{x=NL} \tag{9}$$

Variables N and L refer to the number of cells through thickness, and the layer thickness, respectively. T_P refers to the overall transfer matrix of the entire structure. Since the structure is a complex combination of several features, the unit cell is discretized to derive T_P. We first look at the breakdown of Phase I (Fig. 5Bi). Re-arranged, as shown in Fig. 5Bii, it is clear that Phase I is reminiscent of alternating layers of narrow and wide pores. A clearer illustration is shown in Fig. 5Ci where the excessive parts which do not contribute to this morphology are subtracted away. There are two transfer matrices associated with this region, that for the layer with the narrow pore, T_M, and that for its immediate cavity, T_C. Assuming that this structure is made using a rigid material, the transfer matrix of the narrow pore can be expressed as:

$$T_M = \begin{bmatrix} \cos(k_0 t) & iZ_M \sin(k_0 t) \\ \dfrac{i\sin(k_0 t)}{Z_M} & \cos(k_0 t) \end{bmatrix} \tag{10}$$

For this lattice, the acoustical geometric parameters of concern include the pore length, d, and the pore thickness, t (Fig. 5Cii). Herein, d = 2.16 mm and t = 5.17 mm (Fig. S7). $Z_M = Z_0/d^2$ refers to the normalized impedance of the pore upon first entry into the lattice. The normalization accounts for the reflected waves arising from the abrupt geometrical discontinuity. $Z_0 = \rho_0 c_0$ then refers to the specific acoustic impedance of air, given by the product of the air density (ρ_0) and the aerial speed of sound (c_0). $k_0 = \omega/c_0$ is the acoustic wavenumber, where $\omega = 2\pi f$ is the angular frequency and f refers to frequency. The shape of the cavity, shown in Fig. 5Ci, is then more complicated. Discretizing the cavity into three parts, we can see that the cavity consists of two tapered parts covering the top and bottom and a uniform region in the middle
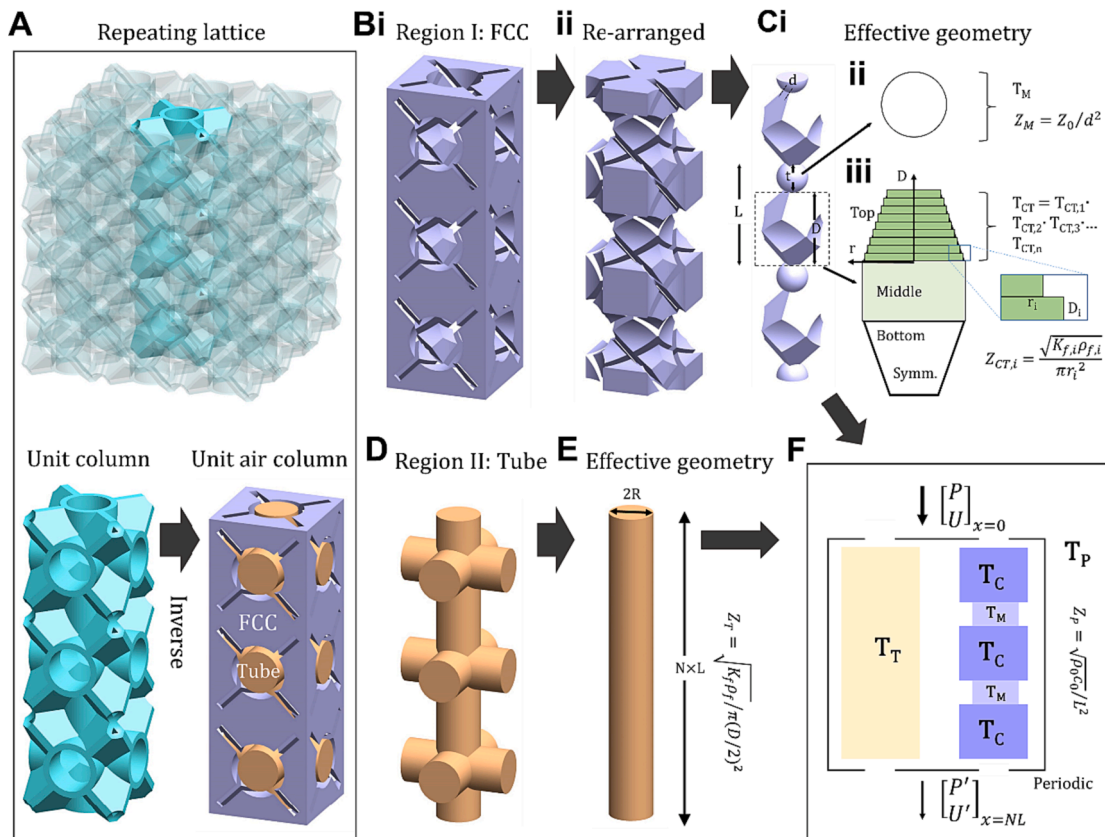

Fig. 5. Discretization of the Iso-PTH for TMM calculations. (A) Illustration of a repeating 3 × 3 × 3 and unit column of the lattice, and a unit column of the air. (B) Region I, representing (i) the FCC phase, and (ii) in its re-arranged state. (Ci) The effective geometry of the FCC phase which contributes to acoustic impedance, (ii) detailed illustration of the cross-section of the narrow pore, and (iii) schematic of the cavity being discretized into infinitesimal portions. The relevant geometrical parameters are included in the same figure. (D) Region II, the SC tube phase, and its (E) effective geometry which contributes to acoustic impedance. (F) A schematic illustration of the combination of the two phases via parallel TMM calculations.

(Fig. 5**Ciii**). Approximating this structure using an infinitesimal number of circular disks, a relationship between the radius (r), and cavity height (D), in terms of millimeters, can be given as:

$$\begin{cases} Top: r = D + 1.5, & 0 \leqslant D \leqslant 3 \\ Middle: r = 6.3, & D = 8.7 \\ Bottom: r = 4.5 - D, & 0 \leqslant D \leqslant 3 \end{cases}$$

This then implies that we can carry out a transfer matrix of an infinitesimal number of circular duct profiles to approximate the matrix, T_C, of the cavity. Herein, the normalized impedance in each layer depends on the effective density (ρ_f), and bulk modulus (K_f) of air through the layer. As a function of ω, the effective density is given as:

$$\rho_f(\omega) = \rho_0 \Big/ \left[1 - \frac{2}{rG_P(\omega)} \frac{J_1(rG_P(\omega))}{J_0(rG_P(\omega))} \right] \tag{11}$$

$$G_P(\omega) = \sqrt{\frac{i\omega\rho_0}{\eta}} \tag{12}$$

The effective bulk modulus is given as:

$$K_f(\omega) = K_0 \Big/ \left[1 - \frac{2(\gamma-1)}{rG_K(\omega)} \frac{J_1(rG_K(\omega))}{J_0(rG_K(\omega))} \right] \tag{13}$$

$$G_K(\omega) = \sqrt{\frac{i\omega Pr\rho_0}{\eta}} \tag{14}$$

The normalized impedance, $Z_{C,i}$, and complex wave number, $k_{C,i}$, through each ith layer is calculated as:

$$Z_{C,i} = \sqrt{K_{f,i}\rho_{f,i}}\Big/\pi r_i^2 \tag{15}$$

$$k_{C,i} = \frac{\omega}{\sqrt{K_{f,i}/\rho_{f,i}}} \tag{16}$$

The matrix of an ith layer, where D_i refers to an infinitesimal layer thickness, is then:

$$T_{Ci} = \begin{bmatrix} \cos(k_{C,i}D_i) & iZ_{C,i}\sin(k_{C,i}D_i) \\ \dfrac{i\sin(k_{f,i}D_i)}{Z_{C,i}} & \cos(k_{C,i}D_i) \end{bmatrix} \tag{17}$$

The matrix of the top profile, T_{CT}, can then be calculated through a transfer calculation across all the layers of the top profile, from D = 0 to D = 3, in infinitesimal i^{th} steps:

$$T_{CT} = T_{CT,1} \cdot T_{CT,2} \cdot T_{CT,3} \dots \cdot T_{CT,i}, \quad i \in \mathbb{Z} \tag{18}$$

Similarly, the matrix of the bottom layer, T_{CM}, can be calculated in a similar way using its own r and D relationship. The matrix of the middle layer is in turn simply the matrix of the circular duct using r = 1.5 and D = 8.7 mm. The total transfer matrix across the cavity is then calculated as:

$$T_C = \prod_{i=1}^{3} T_{Ci} = T_{CT} \cdot T_{CM} \cdot T_{CB} \tag{19}$$

The total transfer matrix, T_H, through region I, then corresponds to the alternating sequence of T_M and T_C:

$$T_H = \prod_{i=1}^{6} T_i = T_M \cdot T_C \cdot T_M \cdot T_C \cdot T_M \cdot T_C \cdot T_M = \begin{bmatrix} t_{h,11} & t_{h,12} \\ t_{h,21} & t_{h,22} \end{bmatrix} \tag{20}$$

Region II takes on the form of an SC truss (Fig. 5**D**). Considering its acoustic impedance, region II can be actually simplified into a simple tube (Fig. 5**E**). The matrix of the tube can be expressed using in a similar way as of Equation (17). Accordingly, the normalized impedance of the tube, calculated using Eqs. (11)–(15), with radius R, is given as $Z_T = \sqrt{K_f\rho_f}/\pi R^2$. The complex wave number, k_T, is then calculated in a

similar way as of Equation (16). The effective length, L_e, through the tube then corresponds to the number of unit cells through thickness, which is $3 \times L$ in this case. T_T is then expressed as:

$$T_T = \begin{bmatrix} \cos(k_T L_e) & iZ_T\sin(k_T L_e) \\ \dfrac{i\sin(k_T L_e)}{Z_T} & \cos(k_T L_e) \end{bmatrix} = \begin{bmatrix} t_{t,11} & t_{t,12} \\ t_{t,21} & t_{t,22} \end{bmatrix} \tag{21}$$

Since regions (I) and (II) are fully separated by the lattice material, i. e., a sound-hard boundary, parallel addition should be considered to model their overall contributions to STL (Fig. 5**F**). Herein, we adopt the parallel TMM method as suggested in the work of Verdiere *et al* [38]. In essence, operations are carried out to combine the final transfer matrices, T_H and T_T, in parallel. For the sake of convenience in mathematical expressions, we first convert the transfer matrices into their admittance matrices, Y_i, for each component M_i placed in parallel:

$$\begin{bmatrix} U(M_i) \\ U(M_i') \end{bmatrix} = Y_i \begin{bmatrix} P(M_i) \\ P(M_i') \end{bmatrix} \tag{22}$$

$$Y_i = \begin{bmatrix} y_{i,11} & y_{i,12} \\ y_{i,21} & y_{i,22} \end{bmatrix} = \frac{1}{t_{i,12}} \begin{bmatrix} t_{i,22} & t_{i,12}t_{i,12} - t_{i,22}t_{i,11} \\ 1 & -t_{i,11} \end{bmatrix} \tag{23}$$

Following this, the overall transfer matrix, T_P, can be calculated by the following transformation:

$$T_P = \frac{-1}{\sum_i^r y_{i,21}} \begin{pmatrix} \sum_i^r y_{i,22} & -1 \\ \sum_i^r y_{i,22}\sum_i^r y_{i,11} - \sum_i^r y_{i,12}\sum_i^r y_{i,21} & -\sum_i^r y_{i,11} \end{pmatrix} = \begin{bmatrix} t_{p,11} & t_{p,12} \\ t_{p,21} & t_{p,22} \end{bmatrix} \tag{24}$$

The constant r_i represents the areal fraction of each of the components. For the Iso-PTH where the SC and FCC phases are superimposed onto each other, i.e., with a same unit cell, r_i for both phases should be equal to 1 in this case [20]. The overall normalized impedance, upon the exit from the lattice, is then $Z_P = \sqrt{\rho_0 c_0}/L^2$. Accordingly, the STL, at each frequency, upon exiting this structure is then calculated through the following expression:

$$STL = 20\log_{10}\left| \frac{1}{2}\left(t_{p,11} + \frac{t_{p,12}}{Z_P} + Z_P t_{p,21} + t_{p,22} \right) \right| \tag{25}$$

Nonetheless, it is worth noting that this numerical model is only valid before the first Bragg frequency [39]. Such types of models are unable to account for dissipation mechanisms arising from lattice cell periodicity.

3.4.3. Effective fluid properties and geometrical influence

The TMM calculated, FEM modelled, and experimentally measured STL curves are plotted together in Fig. 6**A**. Good agreements between the three are observed. The TMM-based microstructure model thus proves to be effective in the modelling of pre-Bragg resonance mechanisms for this lattice structure. We thus use this model with confidence to further investigate the effective fluid properties and the influence of geometrical features. We probe into the frequency dependent effective mass density, ρ_{eff}, of the air in the structure. The overall matrix for the Iso-PTH, T_P, had been derived as shown in Equation (24). Using the elements in this matrix and the dispersion relation [40,41], the effective wavenumber, k_{eff}, and ρ_{eff} can then be derived:

$$k_{eff}(\omega) = \frac{1}{L_e}\sin^{-1}\sqrt{-t_{p,12}t_{p,21}} \tag{26}$$

$$\rho_{eff}(\omega) = \frac{ik_{eff}\sin(k_{eff}L_e)}{\omega t_{p,21}} \tag{27}$$

The frequency dependent plot of ρ_{eff} is shown in Fig. 6**B**. In line with *meta*-acoustic behaviours, negative values are observed at certain frequency ranges. A generally smooth curve lying close to $\rho_{eff} = 0$,
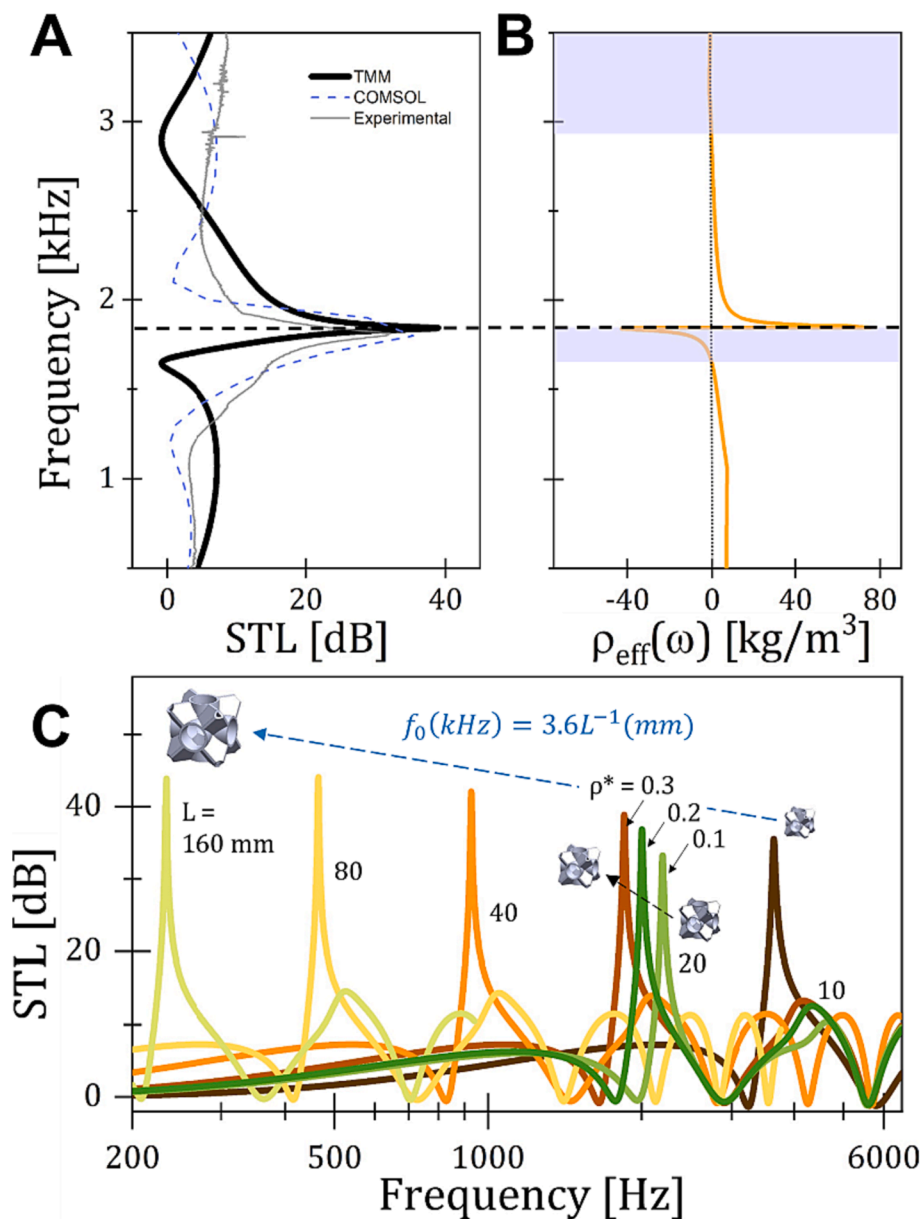
Fig. 6. Further studies from the analytical model. (A) The correlation between the TMM calculated, FEM and experimental STL curves. (B) The calculated effective density of the Iso-PTH, as a function of frequency. (C) The influence of ρ* and cell size on the position of the local resonance peak.

characterized by an abrupt divergence to a highly negative value (1646–1845 Hz), and an abrupt convergence from a large positive value, is observed. This divergence and convergence lie within the peak of the local resonance. Following the first divergence, a second region with a slightly negative ρ_{eff} is observed at a frequency of 2833 Hz onwards. Physically speaking, the highly negative mass corresponds to air volume 180° out of phase with the propagating acoustic wave. High wave attenuation occurs due to this phase difference and a strong wave propagation barrier is thus formed. Indeed, this region corresponds to the region with maximum losses in the STL curve (Fig. 4A).

The TMM analytical model also serves as an analytical tool to derive the STL curve based on solely the lattice geometrical features. We then illustrate the influence of the relative density on the STL attenuation resonant frequency for the Iso-PTH. As shown in Fig. 6C, no distinct differences have been observed. A small peak shift to the right, from 1843 to 2197 Hz, is revealed when ρ* decreases from 0.3 to 0.1. The shift attributes to the lattice acoustical geometric parameters, e.g., d, t, D, and R, varying with the change in relative density. The small shift observed

in turn attributes to the geometrical properties being less influenced by the ρ*, unlike that for truss microlattices [42]. This attributes to geometrical parameters being rather little influenced by ρ*, owing to the high number of features and the plate and tube morphology. Details are summarized in Fig. S7 and Table S1. The influence of the scaling of Iso-PTH, on the STL, is shown also in Fig. 6C. The STL curves of Iso-PTH with L = 10, 20, 40, 80, 160 mm are plotted. Essentially, the relevant acoustical geometric parameters scales linearly in accordance with the cell size. Observable from the logarithm graph, a double in the cell size leads to a halve of the resonant frequency, f_0.

3.5. Customizable acoustics and mechanical properties

From the relationship shown in Fig. 6C, a constitutive inverse power-law relationship to predict f_0, based on the cell size (in terms of kHz and millimeters), can be achieved:

$$f_0 = 3.6L^{-1} \tag{28}$$

For the Iso-PTH, the local resonance can thus be easily predicted given the cell size. As mentioned in Section 3.4.1, the secondary high attenuation region is given by Bragg scattering. Since the numerical model is unable to account for Bragg scattering, we adopt bandgap FEM simulation, in a similar way to that in Fig. 6F,G, to calculate the onset of the Bragg scattering frequency, $f_{B,0}$. The following relationship is derived:

$$f_{B,0} = 9.56L^{-1} \tag{29}$$

Similar to observations for local resonance, and the relation for f_B, the position of a Bragg region halves with a double in the cell size. Following these, considering the unit cell size, L, as a geometrical factor, we can then derive an overall bandgap map for the Iso-PTH across a broad range of cell sizes (Fig. 7A). Assisted using the data points, the local and Bragg bandgaps are marked as the shaded regions. These correspond to regions where no incident sound wave passes through. In the overall map, negative power law relationships (Equations (28),29)) are observed. The local and Bragg's resonance regions also converge closely to each other with the increased cell size. It is worth noting that for any structure, regions beyond the onset of Bragg scattering ($f_{B,0}$) are associated with high sound transmission losses. This is observed in the FEM modelled STL curves in Fig. S8. Therefore, we do not specially specify an end limit to the Bragg scattering region herein. Fig. 7A thus serves as an overall design map for the Iso-PTH, to achieve customized sound insulation properties via tuning the lattice structure cell size. As mentioned, the TMM model is capable of predicting the STL characteristics of any lattice structures that can be discretized. Fig. 7B shows the overall design map of the PTH samples, across the whole range of β. The influences of β on the Young's modulus, isotropy, STL curve are shown. Detailed in Fig. S4, 5, the Young's modulus along [1 0 0] increases with increasing β. Up till β = 0.6, no significant differences to the peak position, and the height, have been observed in the STL curves. The striking difference observed for PTH-0.72 owes to its distinctly narrow cavity. The acoustical geometries of the lattice structures are illustrated in Fig. S9. Beyond the Iso-PTH that we have focused on herein, Fig. 7B also shows that customized mechanical (anisotropy, stiffness) and sound insulation properties, based on β, L, and ρ*, are achievable. Additionally, the degree of sound attenuation is controlled by the number of cells through thickness.

4. Further discussion

Overall, we present a new class of ventilated sound-insulating metamaterial based on lattice structures. Traditionally, sound-insulating materials have been based on fabrics and panels. These materials are however non-ventilating. As a means to improve air flowability, researchers have proposed sonic crystals and acoustic metamaterials based on various resonance mechanisms. However, these structures are limited to being a structure and they do not have the dynamic versatility of a material. For instance, sonic crystals have to be specially erected, and meta-structures can only take on certain geometries. They thus inevitably occupy large spaces. Further, the abovementioned materials are also mono-functional with only sound insulation properties. They are thus often introduced additively as a sound control device to a system or design most of the times. These indirectly imply that additional mass and volume are required in these cases. Our lattice structures can in turn overcome this.

First, as opposed to structures, the lattice structures are in turn regarded to be in the length scale of material. As compared to structures, materials are scalable and versatile. Indeed, the unit cell nature of the lattice allows them to be scalable up to any size, meanwhile being versatile to be implemented into any arbitrary geometry. Secondly, our lattice structure also multi-functions as a strong isotropic structural material, or backup energy-absorbing material, depending on the material used for fabrication. It is capable of reaching around 50–60% of the stiffness of the HS upper bounds for a two-phase isotropic material. These values compare superior to that of isotropic truss lattices [34]. Thirdly, it also displays good sound insulation properties and is air-ventilating (illustrated in Fig. 3B). They compare favourably to various reported acoustic metastructures designed also for sound insulation and air ventilation. At the similar frequency range and a comparable thickness of around 60 mm, it displays higher maximum loss than reported acoustic metacages [11] and spiral metastructures [43]. Comparing their lateral sizes, at a unit cell size of 20 mm, it displays
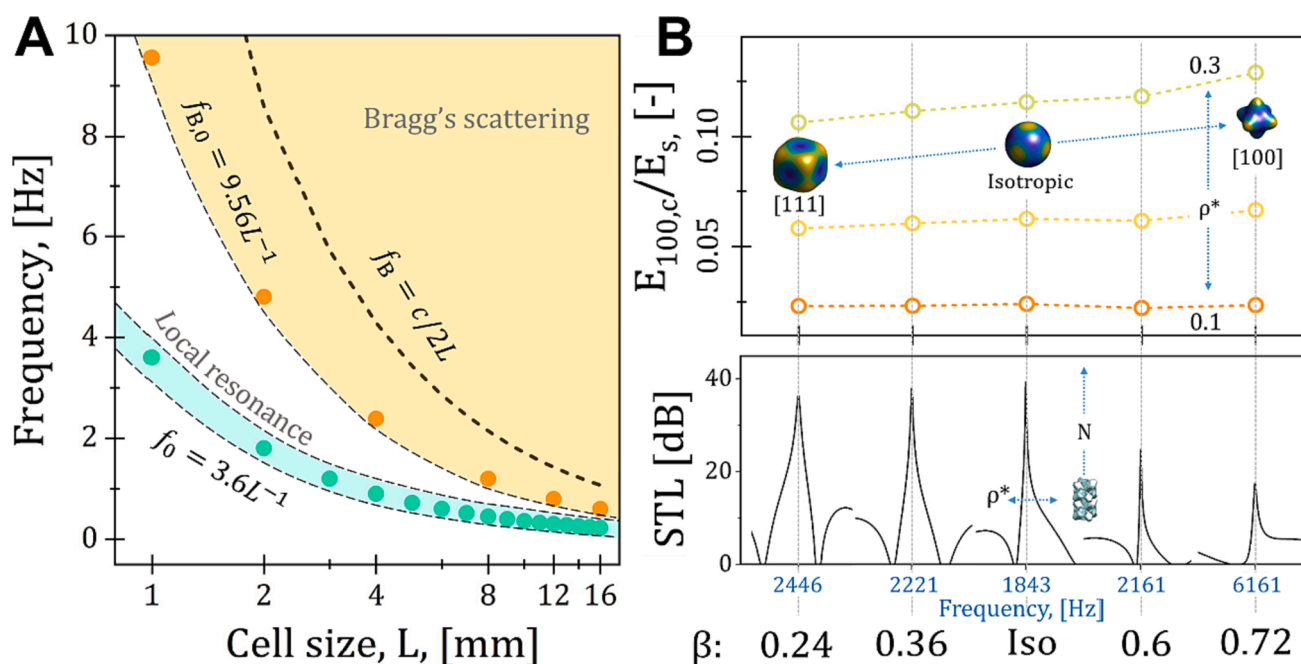

Fig. 7. The customizable acoustics and mechanical properties of the lattice. (A) The overall sound transmissibility map of the Iso-PTH for different cell sizes. The cell size dependent acoustical bandgaps are also plotted onto the same figure. (B) The overall design map of the PTH lattices. The influences of β on the Young's modulus, isotropy, STL resonant frequency and attenuation maximum are shown.

higher maximum losses as compared to *meta*-windows [44]. Lastly, our lattices are customizable for different working environments. From Fig. 7**A,B**, we have illustrated that both mechanical (anisotropy, stiffness) and sound insulation properties, are customizable via simply tuning a few geometrical parameters: β, L, and ρ*. This implies the potential for customized properties depending on the intended working environment.

We have also come up with a TMM-based model for the prediction of STL curves. Apart from this structure, the model can also be used for other similar structures. As can be seen in Section 3.4, the TMM model is built upon combining several discrete lattice features. Therefore, any lattice features can be discretized and be represented using suitable transfer matrices [45]. It is also to note that the model is capable of predicting STL curves to high accuracy (Fig. 5**A**). In other words, we can thus use this model to design lattice structures instead. For instance, to optimize insulation at specific frequency bands, or to optimize heterogeneously porous lattices for broadband sound insulation.

To illustrate its abovementioned design merits, we use sound-proof machinery enclosures as a proof-of-concept (Fig. 1**Di**). Apart from blocking off excessive noises, such enclosures are also required to be air-ventilating to dissipate heat during the machine operation. Traditionally, these enclosures have been proposed using sonic crystals [12] and metastructures [10]. However, it is clear that such structures are unable to function as structural or protection materials. In turn, if the enclosure is to be made using our lattice structure, the enclosure can serve as either a lightweight rigid material (considering the properties presented in Fig. 3**Ci**), or a protective material against impact and crash hazards (Fig. 3**Cii**), both inward and outward from the enclosure. Such a design would find vast applications in the design of aerospace and automobile components. Additionally, our lattices would also serve to function as structural noise barriers that can be implemented along roads for both noise reduction and hazard protection (Fig. 1**Dii**), or as a form of "*meta*-window" that is ventilating (Fig. 1**Diii**). Overall, our lattice displays several simultaneous desirable qualities, including being lightweight, strong, sound-insulating, and air-ventilating. These are all highly sought-after for practical engineering applications. Our lattices are thus expected to find high potentials as advanced multifunctional materials applications requiring these properties, such as in construction, aerospace, and automobile etc.

5. Conclusion

In summary, we have presented a new class of tube-plate hybrid lattice structure as an effective ventilated sound-insulating and structural material. This new structure considers a combination of hollow SC truss and FCC plate lattices. Prior to sound insulation investigations, structural optimization, using a defined structural factor, was carried out to achieve a fully isotropic structure. At a cell size of 20 mm, with three units in the direction of sound wave propagation, the maximum attenuation measures to be 32 dB at a frequency of 1810 Hz. Within this region, a broad insulating region from 1440 to 1950 Hz, where the loss is higher than 10 dB, is present. A secondary high insulation region starts from around 5000 Hz. Investigated through numerical methods, the first onset of attenuation maximum attributes to local Helmholtz resonance while the secondary maximum attributes to the Bragg scattering of the periodic features. Being porous, the lattice is also highly air ventilating where 35% of the airflow can be retained. We have also come up with a high-fidelity microstructure-based analytical model that can be used to predict the STL curve and to illustrate the effective fluid properties. From these, overall design maps for the sound transmissibility and mechanical property are formulated. Simultaneously customizable acoustics and mechanical properties are achievable via tuning a few geometrical parameters of the lattice. The lattice presented in this work thus displays several desirable qualities simultaneously: being lightweight, strong, sound-insulating, and air-ventilating. They are thus expected to find high potentials as advanced multifunctional materials for

applications in aerospace, automobile, and construction. Overall, this work has also successfully proposed a new concept of using lattice structures as sound-insulating materials.

Declaration of Competing Interest

The authors declare that they have no known competing financial interests or personal relationships that could have appeared to influence the work reported in this paper.

Data availability

Data will be made available on request.

Appendix A. Supplementary material

Supplementary data to this article can be found online at https://doi.org/10.1016/j.matdes.2023.112354.

References

[1] S. Kumar, H.P. Lee, Recent advances in acoustic metamaterials for simultaneous sound attenuation and air ventilation performances, Crystals 10 (8) (2020) 686.

[2] N. Gao, Z. Zhang, J. Deng, X. Guo, B. Cheng, H. Hou, Acoustic metamaterials for noise reduction: a review, Adv. Mater. Technol. 7 (6) (2022) 2100698.

[3] F. Morandi, M. Miniaci, A. Marzani, L. Barbaresi, M. Garai, Standardised acoustic characterisation of sonic crystals noise barriers: Sound insulation and reflection properties, Appl. Acoust. 114 (2016) 294–306.

[4] S.M. Dimitrijević, V.M. García-Chocano, F. Cervera, E. Roth, J. Sánchez-Dehesa, Sound insulation and reflection properties of sonic crystal barrier based on micro-perforated cylinders, Materials 12 (17) (2019) 2806.

[5] J. Radosz, Acoustic performance of noise barrier based on sonic crystals with resonant elements, Appl. Acoust. 155 (2019) 492–499.

[6] R.L. Mu, M. Toyoda, D. Takahashi, Sound insulation characteristics of multi-layer structures with a microperforated panel, Appl. Acoust. 72 (11) (2011) 849–855.

[7] J. Yang, J.S. Lee, H.R. Lee, Y.J. Kang, Y.Y. Kim, Slow-wave metamaterial open panels for efficient reduction of low-frequency sound transmission, Appl. Phys. Lett. 112 (9) (2018) 091901.

[8] Y. Cheng, C. Zhou, B. Yuan, D. Wu, Q. Wei, X. Liu, Ultra-sparse metasurface for high reflection of low-frequency sound based on artificial Mie resonances, Nat. Mater. 14 (10) (2015) 1013–1019.

[9] Z. Xiao, P. Gao, D. Wang, X. He, L. Wu, Ventilated metamaterials for broadband sound insulation and tunable transmission at low frequency, Extreme Mech. Lett. 46 (2021) 101348.

[10] C. Liu, J. Shi, W. Zhao, X. Zhou, C. Ma, R. Peng, M.u. Wang, Z. Hang, X. Liu, J. Christensen, N. Fang, Y. Lai, Three-dimensional soundproof acoustic metacage, Phys. Rev. Lett. 127 (8) (2021), 084301.

[11] C. Shen, Y. Xie, J. Li, S.A. Cummer, Y. Jing, Acoustic metacages for sound shielding with steady air flow, J. Appl. Phys. 123 (12) (2018) 124501.

[12] A. Melnikov, M. Maeder, N. Friedrich, Y. Pozhanka, A. Wollmann, M. Scheffler, S. Oberst, D. Powell, S. Marburg, Acoustic metamaterial capsule for reduction of stage machinery noise, J. Acoust. Soc. Am. 147 (3) (2020) 1491–1503.

[13] M. Zhao, X. Li, D.Z. Zhang, W. Zhai, Geometry effect on mechanical properties and elastic isotropy optimization of bamboo-inspired lattice structures, Addit. Manuf. 64 (2023) 103438.

[14] S. Zhao, Y. Zhang, S. Fan, N. Yang, N. Wu, Design and optimization of graded lattice structures with load path-oriented reinforcement, Mater. Des. 227 (2023), 111776.

[15] R. Nam, M. Jakubinek, H. Niknam, M. Rahmat, B. Ashrafi, H.E. Naguib, 3D printed octet plate-lattices for tunable energy absorption, Mater. Des. 228 (2023), 111835.

[16] S. Jiang, D. Guo, L. Zhang, K. Li, B. Song, Y. Huang, Electropolishing-enhanced, high-precision 3D printing of metallic pentamode metamaterials, Mater. Des. 223 (2022), 111211.

[17] K. Liang, Y. Wang, Y. Luo, A. Takezawa, X. Zhang, Z. Kang, Programmable and multistable metamaterials made of precisely tailored bistable cells, Mater. Des. 227 (2023), 111810.

[18] X. Li, X. Yu, J.W. Chua, H.P. Lee, J. Ding, W. Zhai, Microlattice Metamaterials with Simultaneous Superior Acoustic and Mechanical Energy Absorption, Small 17 (24) (2021) 2100336.

[19] X. Li, X. Yu, W. Zhai, Additively manufactured deformation-recoverable and broadband sound-absorbing microlattice inspired by the concept of traditional perforated panels, Adv. Mater. 33 (44) (2021) 2104552.

[20] X. Li, X. Yu, W. Zhai, Less is more: hollow-truss microlattice metamaterials with dual sound dissipation mechanisms and enhanced broadband sound absorption, Small 18 (44) (2022) 2204145.

[21] Z. Li, W. Zhai, X. Li, X. Yu, Z. Guo, Z. Wang, Additively manufactured dual-functional metamaterials with customisable mechanical and sound-absorbing properties, Virtual Phys. Prototyp. 17 (4) (2022) 864–880.

[22] J.W. Chua, X. Li, X. Yu, W. Zhai, Novel slow-sound lattice absorbers based on the sonic black hole, Compos. Struct. 304 (2023) 116434.

[23] J. Boulvert, T. Cavalieri, J. Costa-Baptista, L. Schwan, V. Romero-García, G. Gabard, E.R. Fotsing, A. Ross, J. Mardjono, J.-P. Groby, Optimally graded porous material for broadband perfect absorption of sound, J. Appl. Phys. 126 (17) (2019) 175101.

[24] X. Li, X. Yu, M. Zhao, Z. Li, Z. Wang, W. Zhai, Multi-level bioinspired microlattice with broadband sound-absorption capabilities and deformation-tolerant compressive response, Adv. Funct. Mater. 33 (2) (2023) 2210160.

[25] Z. Li, X. Wang, X. Li, Z. Wang, W. Zhai, New class of multifunctional bioinspired microlattice with excellent sound absorption, damage tolerance, and high specific strength, ACS Appl. Mater. Interf. 15 (7) (2023) 9940–9952.

[26] Z. Li, X. Li, J.W. Chua, C.H. Lim, X. Yu, Z. Wang, W. Zhai, Architected lightweight, sound-absorbing, and mechanically efficient microlattice metamaterials by digital light processing 3D printing, Virtual Phys. Prototyp. 18 (1) (2023) e2166851.

[27] M.J. Prajapati, C. Bhat, A. Kumar, S. Verma, S.-C. Lin, J.-Y. Jeng, Supportless lattice structure for additive manufacturing of functional products and the evaluation of its mechanical property at variable strain rates, Materials 15 (22) (2022) 7954.

[28] X. Zhang, Y. Wang, B. Ding, X. Li, Design, fabrication, and mechanics of 3D micro-/nanolattices, Small 16 (15) (2020) 1902842.

[29] Z. Li, X. Li, Z. Wang, W. Zhai, Multifunctional sound-absorbing and mechanical metamaterials via a decoupled mechanism design approach, Mater. Horiz. 10 (1) (2023) 75–87.

[30] M. Zhao, X. Li, D.Z. Zhang, W. Zhai, Design, mechanical properties and optimization of lattice structures with hollow prismatic struts, Int. J. Mech. Sci. 238 (2022), 107842.

[31] X. Li, M. Kim, W. Zhai, Ceramic microlattice and epoxy interpenetrating phase composites with simultaneous high specific strength and specific energy absorption, Mater. Des. 223 (2022), 111206.

[32] J.B. Berger, H.N.G. Wadley, R.M. McMeeking, Mechanical metamaterials at the theoretical limit of isotropic elastic stiffness, Nature 543 (7646) (2017) 533–537.

[33] S. Xu, J. Shen, S. Zhou, X. Huang, Y.M. Xie, Design of lattice structures with controlled anisotropy, Mater. Des. 93 (2016) 443–447.

[34] T. Tancogne-Dejean, D. Mohr, Elastically-isotropic truss lattice materials of reduced plastic anisotropy, Int. J. Solids Struct. 138 (2018) 24–39.

[35] D. Roca, M.I. Hussein, Broadband and intense sound transmission loss by a coupled-resonance acoustic metamaterial, Phys. Rev. Appl 16 (5) (2021), 054018.

[36] D.P. Elford, L. Chalmers, F.V. Kusmartsev, G.M. Swallowe, Matryoshka locally resonant sonic crystal, J. Acoust. Soc. Am. 130 (5) (2011) 2746–2755.

[37] M.P. Peiró-Torres, S. Castiñeira-Ibáñez, J. Redondo, J.V. Sánchez-Pérez, Interferences in locally resonant sonic metamaterials formed from Helmholtz resonators, Appl. Phys. Lett. 114 (17) (2019) 171901.

[38] K. Verdière, R. Panneton, S. Elkoun, T. Dupont, P. Leclaire, Transfer matrix method applied to the parallel assembly of sound absorbing materials, J. Acoustic. Soc. Am. 134 (6) (2013) 4648–4658.

[39] A. Dell, A. Krynkin, K. Horoshenkov, The use of the transfer matrix method to predict the effective fluid properties of acoustical systems, Appl. Acoust. 182 (2021), 108259.

[40] B.H. Song, J.S. Bolton, A transfer-matrix approach for estimating the characteristic impedance and wave numbers of limp and rigid porous materials, J. Acoust. Soc. Am. 107 (3) (2000) 1131–1152.

[41] P. Li, S. Yao, X. Zhou, G. Huang, G. Hu, Effective medium theory of thin-plate acoustic metamaterials, J. Acoust. Soc. Am. 135 (4) (2014) 1844–1852.

[42] X. Li, Y.H. Tan, H.J. Willy, P. Wang, W. Lu, M. Cagirici, C.Y.A. Ong, T.S. Herng, J. Wei, J. Ding, Heterogeneously tempered martensitic high strength steel by selective laser melting and its micro-lattice: Processing, microstructure, superior performance and mechanisms, Mater. Des. 178 (2019), 107881.

[43] M. Sun, X. Fang, D. Mao, X. Wang, Y. Li, Broadband acoustic ventilation barriers, Phys. Rev. Appl 13 (4) (2020), 044028.

[44] S. Kumar, T.B. Xiang, H.P. Lee, Ventilated acoustic metamaterial window panels for simultaneous noise shielding and air circulation, Appl. Acoust. 159 (2020), 107088.

[45] N. Jiménez, J. Groby, V. Romero-García, Acoustic waves in periodic structures, metamaterials, and porous media, in: Ch. the Transfer Matrix Method in Acoustics, Springer International Publishing, Cham, 2021, pp. 103–164.